1　　# First Performance Results of a New FW-SHS for Geocoronal Hα Research

2　　**D. D. Gardner[1], E. J. Mierkiewicz[2], F. L. Roesler[1], J. M.**
3　　**Harlander[3], K. P. Jaehnig[1], S. M. Nossal[1], and L. M. Haffner[1]**

4　　[1]University of Wisconsin-Madison.[2]Embry-Riddle Aeronautical
5　　University-Daytona Beach.[3]St. Cloud State University

6　　Corresponding author: Derek Gardner (ddgardner@wisc.edu)

7　　**Key Points:**

8　　- FW-SHS instrument extends Hα observations with high resolving power and long
9　　　spectral baseline.

10　　- Field widening prisms allow faint emission detection in compact instrumental design.

11　　- FW-SHS observations are consistent with WHAM observations and coincidently
12　　　obtained Fabry Perot observations.

13　　**Abstract**

14　　A new, high resolution field-widened spatial heterodyne spectrometer (FW-SHS) designed to
15　　observe geocoronal Balmer α (Hα, 6563 Å) emission was installed at Pine Bluff Observatory
16　　(PBO) near Madison Wisconsin. FW-SHS observations were compared with an already well-
17　　characterized dual-etalon Fabry Perot Interferometer (PBO FPI) optimized for Hα, also at PBO.
18　　The FW-SHS is a robust Fourier transform instrument that combines a large throughput
19　　advantage with high spectral resolution and a relatively long spectral baseline (~10x that of the
20　　PBO FPI) in a compact, versatile instrument with no moving parts. Coincident Hα observations
21　　by FW-SHS and PBO FPI were obtained over similar integration times, resolving powers
22　　(~67,000 & 80,000 at Hα) and fields-of-view (1.8 and 1.4 degrees, respectively). Initial FW-SHS
23　　observations of Hα intensity and temperature (Doppler width) vs. viewing geometry (shadow
24　　altitude) show excellent relative agreement with the geocoronal observations previously obtained
25　　at PBO by FPI. The FW-SHS has a 640 km/s (14 Å) spectral bandpass, and is capable of
26　　determining geocoronal Hα Doppler shifts on the order of 100 m/s with a temporal resolution on
27　　the order of minutes. These characteristics make the FW-SHS well suited for spectroscopic
28　　studies of relatively faint, diffuse-source geocoronal Hα emission from Earth's upper
29　　atmosphere (~12-2 R) and the interstellar medium in our Galaxy. Current and future FW-SHS
30　　observations extend long-term geocoronal hydrogen observation data sets already spanning three
31　　solar minima. This paper describes the FW-SHS first light performance and Hα observational
32　　results collected from observing nights across 2013 and 2014.

33　　**Index Terms:** Spatial Heterodyne Spectrometer**,** Exosphere**,** Geocoronal Balmer-alpha,
34　　Interstellar medium

35
36

37

1 Introduction

39

40   A relatively new, novel interferometer for remote sensing upper atmospheric
41 temperatures and dynamics, referred to as a Field-Widened Spatial Heterodyne Spectrometer
42 (FW-SHS, developed at UW-Madison by *Roesler and Harlander* [1990]), has recently been built
43 and field-tested at Pine Bluff Observatory, WI. FW-SHS observations of geocoronal Balmer α
44 (Hα, 6563 Å) airglow and diffuse Galactic Hα recombination emission are compared here to
45 coincidently obtained Fabry Perot Hα observations. The purpose of this paper is to show how
46 FW-SHS geocoronal observations are calibrated and consistent with previously obtained Hα
47 observations, and thus illustrate the precision with which this FW-SHS can extend Hα intensity,
48 temperature and Doppler shift observations from the Earth's upper atmosphere and the Galaxy.
49   Empirical knowledge of upper atmospheric neutral atomic hydrogen is helpful to
50 parameterize boundary conditions for atmospheric coupled climate models, and predict
51 geocoronal depletion and planetary evolution. Here, geocoronal airglow measurements provide
52 useful model validating benchmarks. Ground-based hydrogen airglow observations as forward-
53 model inputs to atmospheric coupled radiative transport models of Hα, allow retrieval and model
54 comparison of relevant exospheric aeronomical parameters such as [H] density and temperature
55 profiles, and vertical hydrogen flux, ϕ_H [e.g. *Bishop* 2001; *Bishop et al*. 2004].
56   Ground-based measurements of geocoronal airglow emission have historically been
57 obtained by Fabry Perot Interferometry, favored for etendue (throughput) and resolving power
58 necessary to fully characterize this diffuse emission line profile. The unique instrumental
59 characteristics of the FW-SHS instrument allow it to surpass the Fabry Perot Interferometers
60 (FPI) in operational versatility and instantaneously sampled bandpass range at similar throughput
61 and resolving powers [e.g., *Harlander et al*., 1992].
62   The SHS in a most basic configuration is similar to a Michaelson Interferometer but with
63 gratings replacing the mirrors in each arm, thus negating the need for mechanical scanning.
64 Spectra are then obtained by Fourier transform of the resulting Fizeau fringes imaged on a CCD
65 detector. Field-widening prisms mounted in each arm further increase the etendue of our SHS,
66 giving it an order-of-magnitude larger sensitivity, on par of that typically obtained by FPI's with
67 a similar effective aperture. Additionally, the FW-SHS is easily transportable and boasts more
68 relaxed optical-flatness defect tolerances than FPI's at similar wavelengths.
69   In this paper we begin with a basic overview of geocoronal Hα line emission, the FW-
70 SHS instrumental concept, specifics of our interferometer, observational strategy and data
71 analysis. Next, we describe our method of spectral and photometric cross-calibration for the FW-
72 SHS interferometer using already established dual-etalon FPI instrumentation (PBO FPI) and
73 Northern Sky Survey data from the Wisconsin Hα Mapper (WHAM) [*Haffner et al.*, 2003]. We
74 conclude with showing first light FW-SHS results obtained with coincident PBO FPI
75 observations, demonstrating instrumental performance, ability to contribute to long-term ground-
76 based geocoronal Hα data sets and aid in retrieval of exospheric dynamical signatures.

77

78

2 Overview of the Geocoronal Hα Line Profile

The solar Lyman β flux scattering off atomic hydrogen in the upper thermosphere and exosphere generates geocoronal Hα fluorescence in a diffuse manner, filling the FOV of our interferometers. As discussed in depth by *Mierkiewicz et al*. [2006], the night-time Hα column emission rate ("intensity") observed from the ground depends on the strength of the Lyman β line center flux, the hydrogen density profile, and observational viewing geometry. Column emission observations are typically categorized by the shadow altitude geometry.

Shadow *altitude* is the radial vector (perpendicular) from ground to the observation point on Earth's shadow that also intersects the line-of-sight shadow *distance* from a ground observer to the same observation point; both are uniquely determined by observational zenith distance, solar depression angle and azimuth. Low shadow altitude geocoronal Hα emission observations (e.g. dawn/dusk) are comparably brightest, being dominated by single-scattering of solar Lyman β near the denser base of the total column emission being observed. Typical FPI zenith observations as a function of shadow altitude show geocoronal Hα intensities ranging from ~12 R near the terminator (~400 km shadow altitude) down to ~2 R looking anti solar-ward into Earth's shadow (>20,000 km shadow altitudes). Multiple scattering of solar Lyman β into Earth's shadow prevents observed geocoronal Hα intensities from approaching zero at high shadow altitudes.

Long term PBO FPI data sets [*Mierkiewicz et al.,* 2006] of low-shadow altitude (<5000 km) geocoronal Hα intensity measurements show a common, general dawn/dusk asymmetry. Zenith dawn measurements are usually brighter by a few Rayleighs (~10-20%) than their dusk counterparts. There is also strong evidence for seasonal variation in Hα intensity [*Tinsley*, 1970] and Hα temperature [*Mierkiewicz et al*., 2012]. Long term (solar cycle) intensity trends and variations, by as much as ~50%, have been discussed in depth by *Nossal et al.* [1993, 2001, 2006, 2008]. Temporal intensity variations have been largely thought attributable [e.g., *Tinsley*, 1970; *Kerr et al*., 2001] to fluctuations in exospheric distribution, content and production of hydrogen, as well as fluctuations in solar Lyman β line center strength.

The geocoronal Hα Doppler emission width is dominated by the temperature near the base of the column emission at the shadow altitude of observation where the solar illuminated column has its highest density. However, the entire column emission contributes to the profile, and due to the range of hydrogen velocity distributions sampled along the column, the distribution is not strictly Maxwellian; therefore temperatures derived from fitting the observed profiles as though they were Maxwellian are referred to as "effective temperatures". As a function of shadow altitude, the geocoronal Hα Doppler width is typically observed to narrow in a near linear fashion from ~7 km/s near the terminator to ~4 km/s at shadow altitudes near 20,000 km [*Mierkiewicz et al*., 2012]. *Kerr et al.* [1986] attributed this narrowing to gravitational cooling of hydrogen.

The spectral line profile of geocoronal Hα fluorescence originates primarily from two solar Lyman β directly-excited fine-structure components that dominate the Hα intensity in a 2 to 1 ratio, along with seven fine-structure cascade transition components due to higher order solar Lyman excitation [*Meier*, 1995]. The overall geocoronal Hα line profile is inherently non-Gaussian. The dominant cascade transition ($3^2S_{1/2} \rightarrow 2^2P_{3/2}$) is redshifted by 6.3 km/s from the dominant directly-excited transition ($3^2P_{3/2} \rightarrow 2^2S_{1/2}$). *Mierkiewicz et al*. [2006] showed that at

123   low shadow altitudes (< 5000 km) the cascade contributions account for 5 (±3)% of the total
124   observed geocoronal Hα emission intensity. At high resolving powers achieved by PBO FPI,
125   *Nossal et al.* [1998] noted the cascade contributions to geocoronal Hα line profile are not
126   negligible, and *Roesler et al.* [2014] show cascade can be constrained by the simultaneously
127   observed intensity of Hβ. When cascade is ignored, effective temperatures retrieved from fits can
128   be overestimated by as much as ~10%.
129   While our PBO FPI and FW-SHS operate at comparable peak signal to noise ratios
130   (SNR) for similar integration times, the FW-SHS longer spectral baseline allows the Hα
131   background emission from the Galaxy to be better characterized and separated from geocoronal
132   emission. Additionally, the presence of multiple Thorium calibration lines across the FW-SHS
133   bandpass allows spectral registration and instrumental profile determination to be quite precise.
134

135   **3 FW-SHS Instrumental Concept**

136

137   The SHS concept (*Harlander et al.* [1992], *Roesler et al.* [2003]) and variations (e.g.
138   *Corliss et al.* [2015], *Lawler et al.* [2008]) are now well described in the literature. Referring to
139   Figure 1, we describe how the instrument works. Collimated and filtered night sky light is fed in
140   (from the right), split at the beam-splitter, and passing through two field widening prisms in
141   nearly-identical path-length arms, the light at frequencies around Littrow wavelength, σ_0, is
142   reflected and dispersed by gratings to be recombined at the beam splitter, exiting towards a
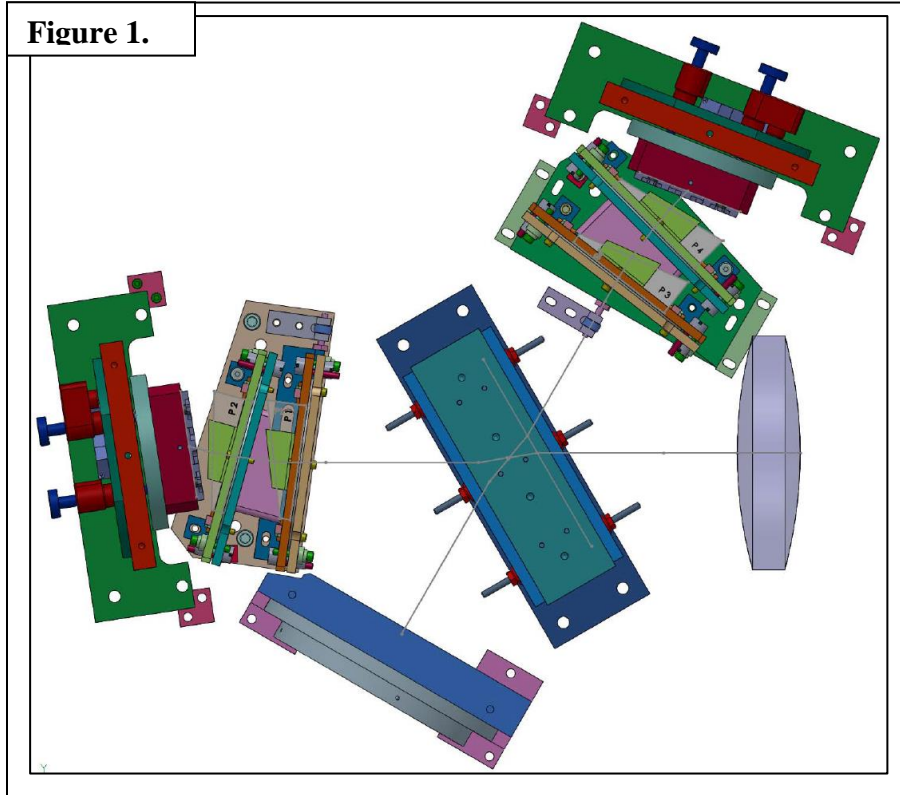143   *single* output.
144

Figure 1.

145

> **Figure 1.** Solid Works instrument model of our FW-SHS. Light enters through the collimating lens on right, to be split at the center beam splitter. *Two* prisms in *each* arm maximize field-widening and minimize aberrations in the high resolution dispersion plane of the gratings (4.2x4.2 cm^2, 600 grooves/mm)

Gratings replacing mirrors in this Michelson-like interferometer setup create a Fizeau fringe interference pattern, localized near the plane of the coincident grating images. Fringes corresponding to wavenumbers $\sigma = \sigma_0 \pm \delta\sigma$ are spatially heterodyned about the user-set Littrow wavelength σ_0 of the gratings, at angle θ. This fringe pattern is recorded by CCD for further Fourier Transform (FT) image processing. Ambiguity between positive and negative spatial frequencies in the FT is eliminated by slightly cross-tilting one grating, breaking the symmetry of the cosine term in equation 1 and *rotating* fringes proportionally to the cross-tilt angle, α. The recorded fringe amplitude is a convolution of the spectral density, $B(\sigma)$, and instrumental profile, $A(x, y, \sigma)$ -- a nearly-frequency-independent line-shape envelope function. A pre-filter and CCD pixel spacing limit the spectral range admitted and observed. In our two dimensional format, the *modulated* spatial fringe intensity can ideally be described by:

$$I(x, y) = \int A(x, y, \sigma)\, B(\sigma)\, \cos[2\pi(\sigma'\, 4\, tan(\theta)\, x + \sigma\alpha\, y)]d\sigma, \qquad (1)$$

where: $\sigma' = (\sigma - \sigma_0)$; the difference is the heterodyned wavenumber in the dispersion dimension (x).

Match pairs of field-widening prisms mounted in each arm allow more off-axis rays to be measured without loss of fringe contrast, increasing the throughput of the interferometer by a factor of ~100. Thus, the input aperture can be opened significantly with minimal distortion of the instrumental line shape profile and centroid drift regularly associated with aperture opening in a traditional FT spectrometer.

Harlander et al. [1992] show the theoretical resolving power of a basic SHS system is R = 4Wσsin(θ), where W is the grating width (4.2 cm), σ is Hα wavenumber (15236.93 cm^{-1}), and θ is the grating Littrow angle at Hα (23.19°). Our system has a theoretical resolving power, R_T = ~100,000. The achieved FW-SHS resolving power after apodization and field-widening is ~67,000 at Hα. At full sensitivity and gain, our FW-SHS can detect single Rayleigh Hα emission brightness from 1.8° FOV sources in about ten minutes at a peak SNR on the order of 50. The 14 Å bandpass (640 km/s at Hα) has a resolution limit of ~4.4 km/s, and with 5x oversampling, a dispersion of ~0.539 km/s /FT pixel bin.

Because the fringes are imaged spatially and each detector element sees light from one small area through the optical train, then fringe phase distortions and line shape errors can be corrected post-acquisition and optical components can have relatively modest tolerances for flatness defects (as compared to Fabry Perot instruments). Phase distortion arising from exit optics and beam splitter aberrations is minimal in our interferometer, and the instrumental profile obtained from the fringe envelope function is quite stable. For Thorium emission lines near Littrow wavelength where Hα was tuned, the phase distortion across the detector was found to be less than a fringe at all path-length differences, even near the interferogram edges. *Englert et al.* [2004] describe mathematical details of SHS distortion correction.

224

4 Observing at PBO

226

227   FW-SHS geocoronal airglow observations were conducted over a two year period (2013
228 & 2014) at Pine Bluff Observatory (PBO, at 43.07° N, 270.33° E). Geocoronal and Galactic Hα
229 observations, mostly obtained by FPI, have been conducted at PBO observing facilities for
230 several decades.
231   The FW-SHS was coupled via fold mirror to a siderostat giving a 1.8° field of view
232 (FOV) target on the sky. Exospheric geocoronal emission is subject to the same atmospheric
233 extinction as Galactic emission; the siderostat's sky tracking accuracy (± 0.1 arc-minute) allowed
234 use of seasonally available nebular sources to correct for atmospheric extinction by the
235 traditional Beer-Lambert approximation. To minimize scattered sunlight, clear weather
236 observations were conducted with solar and lunar depression angles greater than 5° below the
237 horizon.
238   Geocoronal airglow observations towards regions of low Galactic Hα emission (usually
239 high Galactic latitudes, b >30) allow the FW-SHS to observe geocoronal Hα at a sufficient peak
240 SNR ≈ 50 in about ten minutes of CCD integration time. Brighter Galactic regions, near the
241 plane of the Galaxy, could also be targeted for geocoronal observations provided that a sufficient
242 Doppler shift of Galactic Hα emission is obtained to adequately separate and characterize the
243 geocoronal Hα emission.

5 FW-SHS Signal Processing

245

246   The FW-SHS is inherently a Fourier transform instrument. A suite of reduction routines
247 were developed in Interactive Data Language (IDL, v9.6) to FT the geocoronal data and are
248 available upon request. Here we give a brief outline of the reduction pipeline applied to the
249 double-sided FW-SHS interferograms, followed by our line fitting description, and signal to
250 noise definitions.

251   5.1 Data Reduction

252   FW-SHS geocoronal interferograms were integrated on a 512x512 pixel CCD. Cooling to
253 -100°C minimized dark current. In SHS systems in general, the spectral noise is dominated by
254 photon noise multiplexed from the target source; photon shot noise from each spectral element
255 sampled in the bandpass is distributed across the entire interferogram.
256   Each cropped interferogram image (392x350 pixels), is selected for further processing. A
257 CCD bias image is subtracted, and each interferogram is then filtered for cosmic rays. Next, a
258 flat-field image is divided into the interferogram. The flat-field image is constructed by summing
259 continuum images taken with a white light source illuminating the aperture while each
260 interferometer arm is alternatingly blocked. This 'balanced arm' approach [*Englert and
261 Harlander*, 2006] measures the non-modulated part of the SHS interferogram.
262   After flat-fielding, the median interferogram value is subtracted to reduce the DC term in
263 the Fourier transform, and the interferogram is then zero-padded (x5), oversampling the FT for
264 more accurate fitting. The interferogram is apodized using a generalized Hanning function to
265 give a resolving power at Hα of ~67,000. This processed interferogram is Fast Fourier

266 Transformed, and a row cut through 2D power spectrum (the modulus of FT) in the lower half
267 plane gives the spectrum; the upper half plane, by virtue of the grating cross-tilt angle, gives
268 identical spectral information and is ignored. Lastly, emission spectra are corrected for the
269 instrumental Hα filter response by dividing the spectrum through by a smoothed continuum
270 spectral response obtained from a white light source.

271   5.2 Hα Line Profile Fitting

272   Spectra at this point are now ready to be fit using our VoigtFit (VF) model, a macro
273 package for Fudgit, developed by *Woodward* [2013]. The VF model is a least-squares chi-
274 minimization analysis program that allows multiple Voigt profiles (and background) to be fit to 1
275 dimensional data. In particular, VF allows each Voigt line parameter (e.g., width, area, center) to
276 be constrained (linked) to other Voigt lines (e.g., line intensity *ratios* can be held constant in the
277 model fit to the data). Experimentally determined instrumental profiles are convolved with the
278 model fit, such that de-convolved empirical data parameters may be retrieved.
279   Geocoronal Hα emission spectra are fit in VF using *Meier*'s [1995] atomic parameters to
280 link Hα fine-structure components' relative areas, widths, and centers. A first fit cluster links the
281 two solar Lyman β excited (direct) fine structure transition's (3P → 2S) *relative* intensities. A
282 second fit cluster links fine structure cascade transition intensities similarly. The cascade (to
283 total) intensity ratio has been fixed to *Roesler et al.*'s [2014] empirically determined value of
284 4.5% for the observational shadow altitudes probed here.
285   Galactic Hα emission in geocoronal spectra are accounted for in our VF models by
286 linking (constraining) the *relative* intensities and Doppler shifts for Galactic components present
287 in each observation using data from WHAM's Northern Sky Survey [*Haffner et al.*, 2003].
288 Galactic component intensity ratios were determined by flux weight averaging intensities already
289 sampled by WHAM to our FW-SHS's larger FOV.

290   5.3 Signal to Noise

291   To compare the PBO FPI and FW-SHS coincident geocoronal spectra, we use a local
292 (peak) signal to noise ratio (SNR) estimate in the spectral domain, defined below for both
293 instruments. We also compare instrumental performance with the fitted line areas divided by the
294 uncertainty in the fit, referred to as the "fit SNR".
295   *Mierkiewicz et al.* [2006] and *Coakley et al.* [1996] show the local SNR ratio for a Fabry
296 Perot system can be estimated, as,
297

$$\frac{S}{N}_{est} = \frac{Lcp}{\sqrt{Lcp + Bcp + DTp + R_n^2 p}}, \quad (2)$$

298
299 where *L* is the recorded number of analog-to-digial (ADU) counts per pixel on the line
300 (multiplied by 0.8, the average line transmittance within *fwhm*), and *B* is the background ADU,
301 recorded in time *T* in seconds, at an effective gain of *c* (photoelectrons/ADU), and *p* is the
302 number of pixels annularly summed into one resolution element (or bin). *D* and *R* are the
303 measured dark current and r.m.s. read noise.
304   *Davis et al.* [2001] and *Harlander* [1991] show that the local SNR for a Fourier
305 Transform instrument can be estimated as,
306

$$\frac{S}{N_\sigma} = \frac{B(\sigma)}{\epsilon_\sigma}, \qquad (3)$$

307

308   where $B(\sigma)$ is the peak signal in the spectral domain, and ϵ is the r.m.s. noise.

309   FW-SHS instrumental signal to noise may be estimated in either the spectral or

310 interferogram domain by counting photons. Since we operate in the photon shot noise limit in the

311 interferogram domain, and the FT of white noise *is* white noise, we can estimate the noise

312 present by taking the r.m.s. value of FT "off-row" |A| (where no amplitude, A, is present in the

313 2D FT by virtue of the grating cross-tilt angle) as a representation of the local white noise in our

314 spectra.

315

316 **6 Photometric Calibration**

317

318   A traditional Hα calibration target used to calibrate both WHAM and PBO FPI, is

319 NGC7000 (i.e., the North American Nebula). Using standard stellar sources, *Scherb* [1981]

320 calibrated a 0.8° FOV portion of NGC7000, centered at α(1950)=20^h 56^m 17^s, δ(1950)=44° 24'

321 03'', with Hα surface brightness of 850 ± 50 R. Using WHAM's FPI (spectral baseline ~200

322 km/s at Hα), *Haffner et al.* [2003] calibrated the same NGC7000 look direction at a 1.0° FOV

323 with Hα surface brightness of 800 ± 50 R (NGC7000 is *not* spatially uniform). Using the FPI at

324 PBO (spectral baseline ~75 km/s at Hα), *Mierkiewicz et al.* [2006] extended the photometric

325 calibration of NGC7000 to a FOV of 1.4° with Hα surface brightness of ~650 R. By targeting

326 the same patch of sky at alternating FOV's, the FW-SHS photometric response can be obtained

327 by similarly bootstrapping to a 1.8° FOV. FW-SHS data for this direct calibration method is

328 currently being reduced (not presented here).

329   Since NGC7000 is not always available, we developed an alternative nightly calibration

330 method using existing Galactic Hα data from WHAM. Galactic regions of known Hα intensity

331 were targeted that spatially fill the FW-SHS FOV as uniformly as possible. The photometric

332 response of the FW-SHS instrument to Hα emission could then be statistically estimated using

333 WHAM's Northern Sky Survey database by geometrically weighting the Galactic Hα flux

334 sampled by WHAM towards the same look-direction within the FW-SHS larger FOV.

335   Flux weighted calculations of intensity reproduced all above listed intensities for

336 NGC7000 at varying FOVs, within ± 50 R. Thus, Galactic Hα emission in an FW-SHS spectrum

337 could be reliably estimated to provide a useful photometric calibration of the geocoronal Hα

338 emission:

339

$$I_{SHS} \cong \frac{1}{\Omega_{SHS}} \sum_i I_i' \Omega_i + \varepsilon, \qquad (4)$$

341

342 where $I_i' \Omega_i$ is the partial flux of each 1° WHAM beam sampled within Ω_{SHS}=1.8° FOV of the

343 FW-SHS; here, ε is the flux-weighted error approximation for FOV within FW-SHS observation

344 not directly sampled by WHAM – to zeroth order it may be taken as the average flux multiplied

345 by the FOV ratio, $\Omega_{not\ covered} / \Omega_{covered}$.

346   The FW-SHS was also directly cross calibrated with the already-calibrated PBO FPI.

347 *Mierkiewicz et al.* [2006] demonstrated the absolute photometric response of the PBO FPI to the

348 near spatially uniform geocoronal Hα emission, so the FW-SHS response could be directly
349 obtained by comparing geocoronal Ha emission line areas. Zenith Hα observations were
350 obtained simultaneously by PBO FPI and FW-SHS during the summer and fall of 2014 for this
351 purpose, and to also validate the WHAM data estimation method above.
352

353 **7 Spectral Calibration**

354

355   A Thorium Argon (ThAr) hollow cathode lamp was used each observing night to
356 spectrally register geocoronal Hα emission and to calibrate the FW-SHS dispersion. Hourly
357 ThAr were needed to register sky spectra due to slow room temperature fluctuations inducing
358 small grating and exit optic thermal shifts in our open air interferometric setup. The resulting
359 spectral shifts of ThAr line peaks between successive spectra, across a few resolution elements,
360 were linearly interpolated through time to retrieve absolute peak spectral positions in geocoronal
361 observations taken between lamp readings.
362   FW-SHS gratings were tuned so that the Hα emission (6563 Å) fell within a few
363 Angstroms of the Littrow wavelength. Across the filter-corrected 14 Å bandpass, five Thorium
364 emission lines were then available for dispersion calculation (6558, 6560, 6564, 6565, 6569 Å).
365 Thorium emission at typical hollow cathode lamp temperatures ~1000 K has an estimated line
366 width of 0.4 km/s [*Mierkiewicz et al.*, 2006], an order of magnitude lower than the FW-SHS
367 resolution limit (~4.4 km/s is the FW-SHS observed width of ThAr 6564 Å emission line, with
368 apodization). Thus, Thorium emission can be used as an effective delta-function input to retrieve
369 the FW-SHS instrumental profile (IP). The 6564 Å Thorium emission line, nearest the Littrow
370 wavelength and Hα, was used as the true IP. This symmetric IP was convolved in the fitting of
371 geocoronal Hα spectra to differentiate true Hα emission width from instrumental broadening.
372   The magnitude of errors in fitted spectral line positions, in absence of thermal drifts, give
373 our FW-SHS an estimated Doppler shift detectability limit on the order of 100 m/s. *Davis et al.*
374 [2001] remind us FTS instruments in the photon noise dominated applications can potentially
375 achieve uncertainties in spectral line positions roughly equal to the ratio of the $fwhm/(SNR_\sigma \times$
376 $\sqrt{N_s})$. E.g., with average Hα line width (*fwhm*) of ~5.5 km/s, a peak SNR on the order of 50,
377 and a minimally sampled number of points in the line width, N_s ~6, gives an estimate of the
378 Doppler shift detectability to an order of 50 m/s.
379

380 **8 First Light Results**

381

382   Coincident geocoronal observations by the PBO FPI and FW-SHS were conducted to
383 assess instrumental performance, demonstrating the FW-SHS utility for geocoronal research.
384 Figure 2 illustrates the utility of the FW-SHS baseline for isolating the entire Galactic
385 background; narrower spectral baseline instruments designed for geocoronal Hα observations,
386 e.g. the PBO FPI, must rely on extrapolation outside their bandpass to fit large red-shifted
387 Galactic Hα components. Figure 2 a (& b) is the interferogram (and 2D FT) of an FW-SHS
388 observation towards NGC1499, processed as described above. The resulting FW-SHS spectrum
389 is shown in Figure 2c; the dispersion is negative (spectrum goes from red to blue). In addition to

396   sampling geocoronal Hα emission, the FW-SHS also samples OH airglow emission (near 120
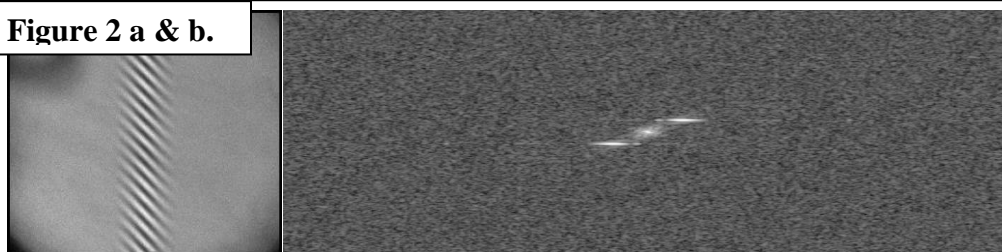397   km altitude).
398

Figure 2 a. (left) 392x350 pixel FW-SHS fizeau-fringe interferogram of well-resolved Hα emission from NGC1499 obtained 02/22/14 from PBO, showing selected region to be fourier transformed.
Figure 2 b. (right) FT symmetry is broken by a small grating cross tilt (a tilt perpendicular to the dispersion plane), so the NGC1499 spectrum (Figure 2 c) can be obtained from the lower half plane cut through the 2D power spectrum.
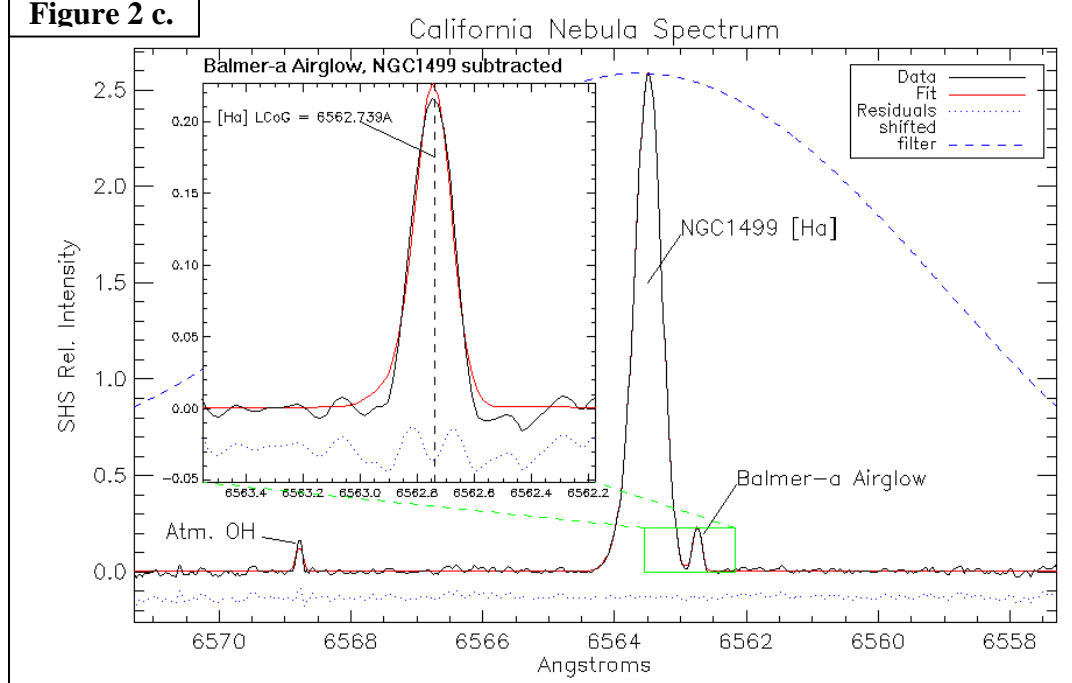
Figure 2 c. a 2 minute Hα FW-SHS exposure, at 1.8° FOV, towards NGC1499 obtained 02/22/14 (vlsr +35.5 km/s). The filter response to broad spectrum white light source is over-plotted & divided into each raw spectrum, giving an effective bandpass of 14 Å. Galactic Hα intensity from NGC1499 is ~230 Rayleighs. (inset) FW-SHS resulting Hα airglow spectrum with Galactic background removed, confined to PBO FPI spectral range (green box, ~65 km/s) illustrating the utility of FW-SHS's spectral baseline grasp to fully sample and separate geocoronal and Galactic Hα emission.

412
413
414   Figure 3 and 4 show ten minute coincident zenith observations from the FW-SHS and
415   PBO FPI, taken at the same time near local midnight on 09/22/14 (at an observational shadow
416   altitude of 3100 km, and vlsr = -29.7 km/s). Black traces are data, red solid traces are the
417   retrieved fits, and over-plotted dashed blue traces are the known Galactic components
418   comprising the fits.
419
420

Figure 3.   FW—SHS Geocoronal Spectrum
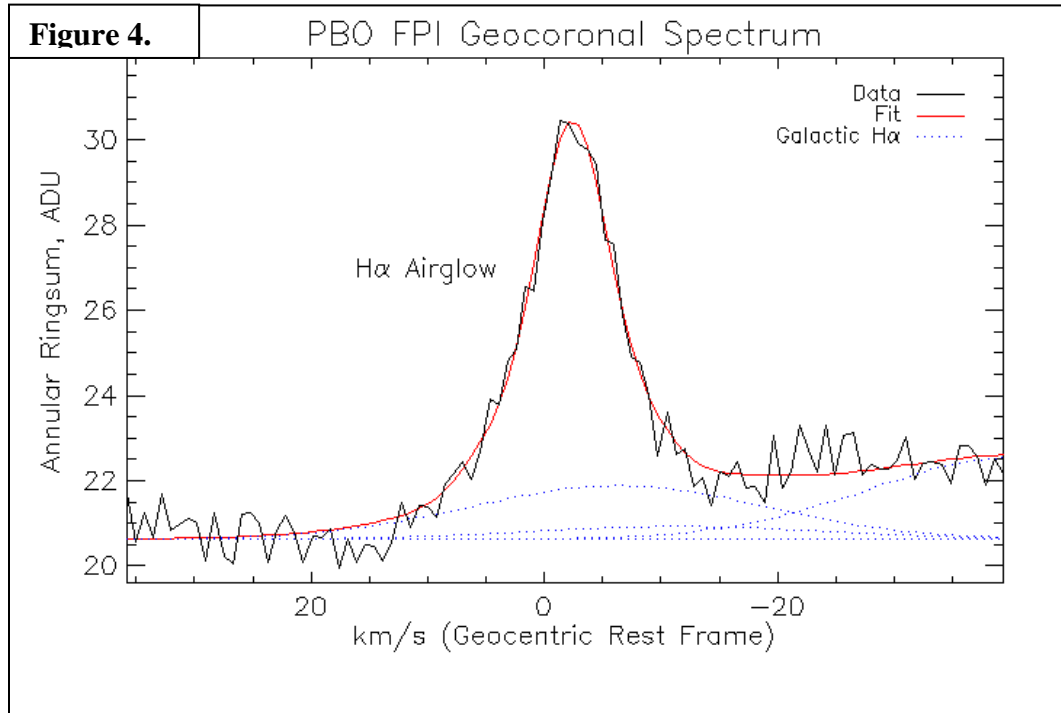
421
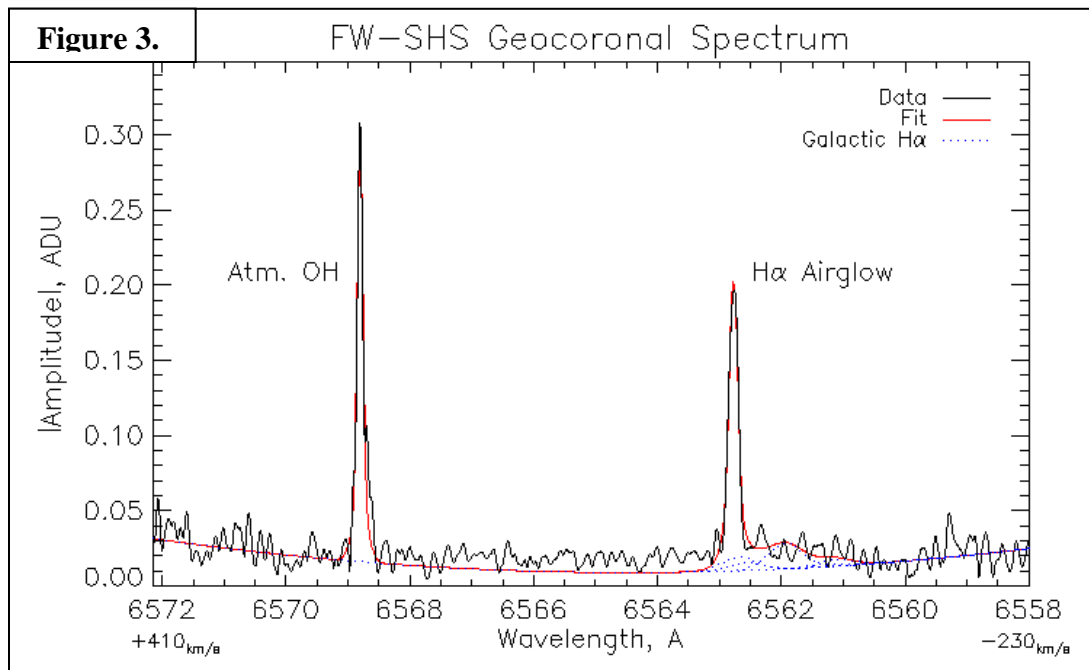
Figure 4.

Figure 3 & 4. Geocoronal FW-SHS spectrum and coincidently obtained PBO FPI spectrum, respectively. Using the already-calibrated PBO-FPI's response to the geocoronal Hα emission, or by using the calibrated WHAM Galactic Hα emission, the FW-SHS observed Hα emission intensity can be determined. Both FW-SHS and PBO FPI agree that the geocoronal Doppler emission width is 4.9 km/s, a typical value for this observational shadow altitude (3100 km).

441

442
443

444   Referring to Eq. (2) and Figure 4, our PBO FPI's CCD operates at c=1.22
445   photoelectron/ADU, R=7 e⁻/pixel, and D=0.001 e⁻/pixel/s. The PBO FPI geocoronal Hα
446   spectrum was retrieved by annularly summing the observed ring image obtained on CCD
447   [*Coakley et al.*, 1996]; p=336 pixels were summed into the resolution element at the geocoronal
448   line peak. At an integration time of 600 s, we recover a peak SNR ≈ 53 and a fit SNR is ≈ 46.
449   Our FW-SHS CCD operates at a lower read noise (4.8 e⁻/pixel), higher gain (1.42
450   photoelectron/ADU), and similar dark current as the PBO FPI CCD, but all negligible since we
451   are dominated by photon multiplexed noise. The r.m.s. noise level in this FW-SHS spectrum was
452   0.0135. With Eq. (3), at an integration time of 600 s, the recovered peak SNR ≈ 16 but the fit
453   SNR is ≈ 460 owing to the FT reduction's 5x oversampling.
454   WHAM data for this look direction coincidently probed by FW-SHS & PBO FPI
455   (Figures 3 & 4) suggests there are several faint (< 1 R) and wide (~40 km/s) Galactic Hα
456   emission components near the geocoronal Hα emission. Referring to the inset WHAM map in
457   Figure 5, Eq. 4 predicts Galactic Hα intensity ≈ 2.6 R. The complete Galactic component's
458   background emission is evident in the FW-SHS spectrum, but only partially seen by the shorter
459   spectral baseline of the PBO FPI. Thus, in this example spectrum the PBO FPI *overestimates* the

451 Galactic Hα intensity (here, by a factor of ~2.46) when extrapolating WHAM-derived fit
452 components beyond the available spectral range.
453   The well-calibrated PBO FPI intensity response suggests the geocoronal Hα emission
454 intensity coincidently observed by the FW-SHS was 3.7 R – an expected value for the
455 observational shadow altitude probed. In our FW-SHS spectrum, cross multiplying the total
456 Galactic fit area by the ratio of the PBO FPI calibrated geocoronal emission to FW-SHS
457 geocoronal area, R/area, suggests the FW-SHS observed Galactic background is 2.8 R – nearly
458 identical to what WHAM predicts (2.6 R).
459   This implies the observed FW-SHS geocoronal emission intensity can be determined
460 reasonably well using background Galactic Hα emission already present in the FW-SHS
461 spectrum and WHAM data alone (via Eq. 4). The WHAM-derived predicted geocoronal Hα
462 intensity observed by the FW-SHS is 3.4 R. The small difference (0.3 R) from what the PBO FPI
463 predicts for the geocoronal intensity is likely due to noise affecting fits and also possibly spatial
464 non-uniformity of surface brightness emission in the actual observed Galactic region, as
465 compared to the WHAM data estimate based on 1° FOV sampling (see Figure 5, inset map).
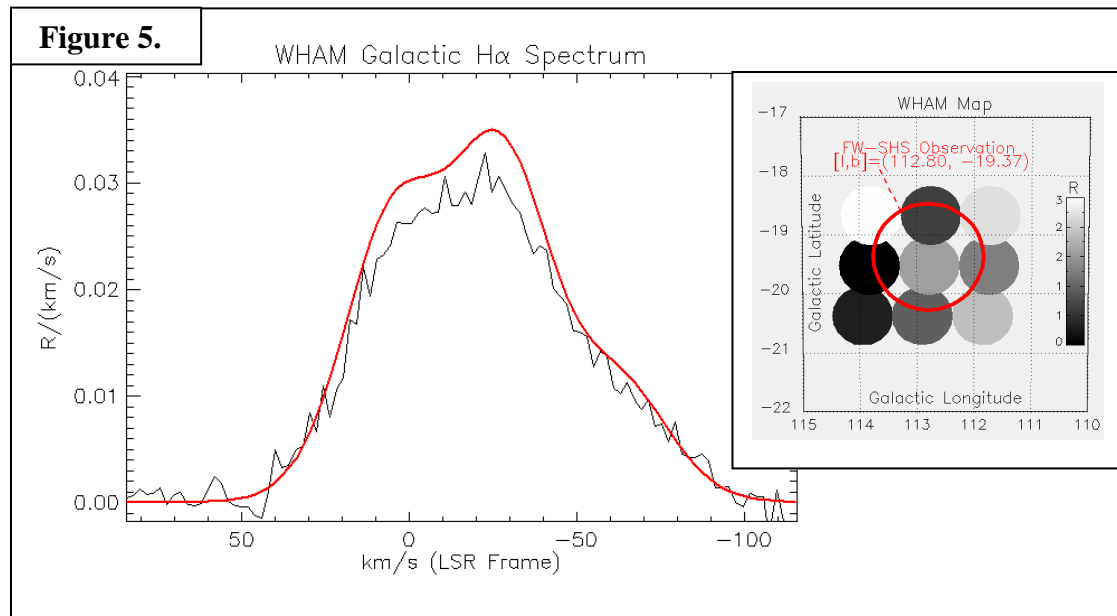466
467

Figure 5.

468

Figure 5. WHAM spectrum of Galactic Hα emission for look direction
coincidently probed by FW-SHS & PBO FPI (Figures 3 & 4). The black trace is the
average raw Galactic spectrum of each WHAM beam sampled near the coincident
observation's Galactic coordinates. The red trace is a more accurate, flux-weighted
spectral estimate (by Eq. 4), accounting for spatial variation of each WHAM
beam's components within our FW-SHS's larger FOV (over-plotted red circle on
inset WHAM map of 1° FOV intensities, projected on normalized grey-scale).

469
470

471   A collection of coincident PBO FPI and FW-SHS zenith observations, with very low
472   Galactic emission, allow a geocoronal calibration curve of (known PBO FPI) emission intensity
473   vs shadow altitude to be constructed; this is shown in Figure 6. Intensities were obtained by
474   integrating emission ±10 km/s around geocoronal peaks in both instrument's spectra, and
475   *assuming* negligible (flat) Galactic background. As anticipated, the FW-SHS (red points) shows
476   good relative agreement in photometric response with the PBO FPI (green points). Knowing the
477   absolute photometric response of the PBO FPI, the FW-SHS photometric response at Hα can be
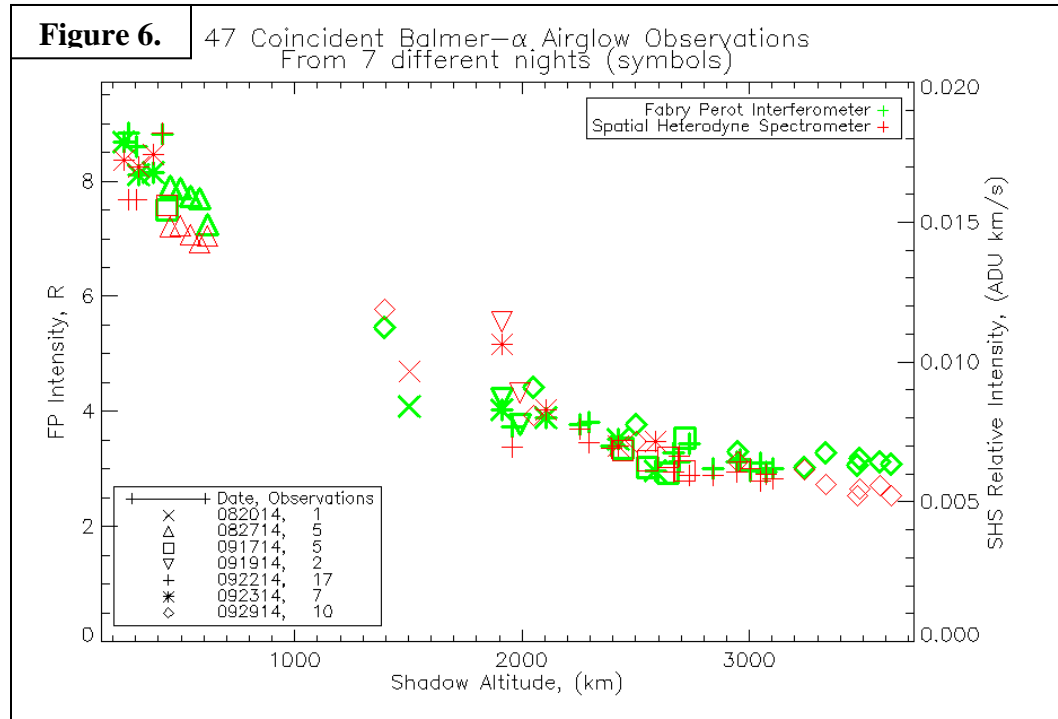478   retrieved.
479

Figure 6. FW-SHS observations of geocoronal Hα airglow intensity (red) vs.
viewing geometry (i.e., shadow altitude) show relative response agreement
with coincidently obtained PBO FPI (green) observations. Intensities were
obtained by integrating emission 10 km/s around geocoronal peaks in both
instrumental spectra, and *assuming* negligible (flat) Galactic Hα emission.

481
482

483   From previously obtained and calibrated PBO FPI data [*Mierkiewicz et al.* 2006],
484   geocoronal Hα airglow is known to fall from 12 (±3) R and plateau near ~2 R across the plotted
485   range of shadow altitude. The break in Figure 6 data, between ~1000 to 2000 km shadow
486   altitudes, is due to Galactic plane passing overhead during coincident zenith observations
487   conducted in Fall of 2014; those geocoronal data points could not be simply reduced with a
488   constant background assumption. But, as previously described with Figures 3 & 4, careful
489   component fitting of this Galactic Hα emission can provide additional photometric calibration
490   via the WHAM data set itself.
491

9 Conclusions

In this paper first light results were presented illustrating the FW-SHS interferometer's performance investigating geocoronal Hα emission. Emission as faint as a single Rayleigh can be observed within ten minutes at a spectral resolving power near to, and sensitivity typical of, FPI's used for geocoronal work. In particular, the FW-SHS instrument's relatively long spectral baseline allows better characterization of background Galactic Hα emission in geocoronal spectra, as well as a robust spectral calibration to register sky spectra.

We also showed that the WHAM Galactic data can be used to calibrate the terrestrial hydrogen airglow observations taken by the FW-SHS instrument, and validated this by cross comparison with the already calibrated PBO FPI. This method can be applied to the calibration of Hα observations made with other interferometers, especially during times of the year when the standard North American Nebula source is not observable or when the instrument does not have pointing capabilities to observe nebular sources. The uncertainty in this photometric calibration method (using WHAM data alone) is ultimately determined by the FW-SHS obtained SNR in each observation and the uncertainty in the WHAM data itself (~10%, conservatively). Additionally, the agreement of the FW-SHS observed geocoronal intensity as derived by either coincident PBO FPI geocoronal observation or WHAM Galactic data (constraining Galactic emission in the FW-SHS spectra) corroborates the two independent calibration methods used for WHAM and the PBO FPI.

The FW-SHS is currently being redeployed from PBO to Daytona Beach, Florida (ERAU). It will be integrated along with a suite of SHS and FPI instruments in a new, remotely operable and transportable optical observatory ("INSpIRe") for investigations of near space weather and upper atmospheric airglow phenomena.

References

Bishop, J. (2001), Thermospheric atomic hydrogen densities and fluxes from dayside Lyman α measurements, *J. Atm. & Sol.-Terr. Phys.*, *63*, 331-340

Bishop, J., E.J. Mierkiewicz, F.L. Roesler, J.F. Gomez, C. Morales (2004), Data-model comparison search analysis of coincident PBO Balmer α, EURD Lyman β geocoronal measurements from March 2000, *J. Geophys. Res.*, *109*, A05307, doi:10.1029/2003JA010165

Coakley, M.M., F.L. Roelser, R.J. Reynolds, S. Nossal (1996), Fabry-Perot/CCD annular summing spectroscopy: study and implementation for aeronomy applications, *Appl. Opt.*, *35*, 6479-6493

533 Corliss, J.B., Harris, W.M., Mierkiewicz, E.J., Roesler, F.L. (2015), Development and field tests
534   of a narrowband all-reflective spatial heterodyne spectrometer, *Appl. Opt., 54*(30), 8835-
535   8843

536 Davis, S.P., M.C. Abrams, J.W. Brault (2001), *Fourier Transform Spectrometry*. Academic, San
537   Diego, CA.

538 Englert, C.R., J.M. Harlander, J.G. Cardon, F.L. Roesler (2004), Correction of phase distortion in
539   spatial heterodyne spectroscopy, *Appl. Opt.*, *43*(36), 6680-6687

540 Englert, C.R., and J.M. Harlander (2006), Flatfielding in spatial heterodyne spectroscopy, *Appl.
541   Opt.*, *45*(19), 4583-4590

542 Haffner, L.M., R.J. Reynolds, S.L. Tufte, G.J. Madsen, K.P. Jaehnig, J.W. Percival (2003), The
543   Wisconsin H-Alpha Mapper Northern Sky Survey, *Astrophys. J.S.*, *149*(2), 405-422

544 Harlander, J.M. (1991), Spatial Heterodyne Spectroscopy: interferometric performance at any
545   wavelength without scanning, Ph.D. thesis, Univ. of Wisconsin-Madison, Madison,
546   Wisconsin, USA

547 Harlander, J.M., R.J. Reynolds, F.L. Roesler (1992), Spatial heterodyne spectroscopy for the
548   exploration of diffuse interstellar emission lines at far ultraviolet wavelengths, *Astrophys.
549   J.*, *396*, 730-740

550 Kerr, R.B., S.K. Atreya, J.W. Meriwether, C.A. Tepley, R.G. Burnside (1986), Simultaneous H a
551   line profile and radar measurements at Arecibo, *J. Geophys. Res.*, *91*, 4491-4512

552 Kerr, R.B., R. Garcia, X. He, J. Noto, R.S. Lancaster, C.A. Tepley, S.A. Gonzalez, J. Friedman,
553   R.A. Doe, M. Lappen, B. McCormack (2001), Periodic variations of geocoronal Balmer-
554   alpha brightness due to solar-drive exospheric abundance variations, *J. Geophys. Res.*,
555   *106*(A12), 28797-28817

556 Lawler, J.E., Z.E. Labby, J.M. Harlander, F.L Roesler (2008), Broadband, high-resolution spatial
557   heterodyne spectrometer, *Appl. Opt., 47*(34), 6371-6384

558 Meier, R. R. (1995), Solar Lyman series line profiles and atomic hydrogen excitation rates,
559   *Astrophys. J.*, *452*, 462-471, with Erratum (1996), *Astrophys. J.*, 468, 455

560 Mierkiewicz, E.J., F.L. Roesler, S.M. Nossal, R.J. Reynolds (2006), Geocoronal hydrogen
561   studies using Fabry-Perot interferometers, part 1: Instrumentation, observations, and
562   analysis, *J. Atm. & Sol.-Terr. Phys.*, *68*, 1520-1552

563 Mierkiewicz, E.J., F.L. Roesler, S.M. Nossal (2012), Observed seasonal variations in exospheric
564   effective temperatures, *J. Geophys. Res.*, *117*, A06313, doi:10.1029/2011JA017123

565 Nossal, S.M., R.J. Reynolds, F.L. Roesler, F. Scherb (1993), Solar cycle variations of geocoronal
566   Balmer α emission, *J. Geophys. Res.*, *98*, 3669-3676

567 Nossal, S.M., F.L. Roesler, M.M. Coakley (1998), Cascade excitation in geocoronal hydrogen
568   Balmer-α line, *J. Geophys. Res.*, *103*(A1), 381-390

569 Nossal, S.M., F.L. Roesler, R.J. Reynolds, M. Haffner, S. Tufte, J. Bishop, J. Percival (2001),
570   Geocoronal Balmer a intensity measurements using the WHAM Fabry-Perot facility, *J.
571   Geophys. Res. 106*, 5605-5616

572 Nossal, S.M., E.J. Mierkiewicz, F.L. Roesler, R.J. Reynolds, L.M. Haffner (2006), Geocoronal
573   hydrogen studies using Fabry-Perot interferometers, part 2: Long-term observations, *J.
574   Atm. & Sol.-Terr. Phys.*, *68*, 1553-1575

575 Nossal, S.M., E.J. Mierkiewicz, F.L. Roesler, L.M. Haffner, R.J. Reynolds, R.C. Woodward
576   (2008), Geocoronal hydrogen observations spanning three solar minima, *J. Geophys.
577   Res.*, *113*, A11307, doi:10.1029/2008JA013380

578 Roesler, F.L., and J.M. Harlander (1990), Spatial Heterodyne Spectroscopy: interferometric
579   performance at any wavelength without scanning, *Proc. SPIE*, *1318*, 234-243
580 Roesler, F.L., J.M. Harlander, J.G. Cardon, C.R. Englert, R.J. Reynolds, K. Jaehnig, S.
581   Watchorn, E.J. Mierkiewicz, J. Corliss (2003), Spatial Heterodyne Spectroscopy: An
582   emerging technology for interference spectroscopy, in *Hubble's Science Legacy: Future
583   Optical-Ultraviolet Astronomy from Space, ASP Conf. Ser.,* vol. 291, edited by K.R.
584   Sembach et al., pp. 395-398
585 Roesler, F.L., E.J. Mierkiewicz, S.M. Nossal (2014), The Geocoronal Hα Cascade Component
586   determined from Geocoronal Hβ Intensity Measurements, *J. Geophys. Res. Space
587   Physics*, *119*, 6642-6647
588 Scherb, F. (1981), Hydrogen production rates from ground-based Fabry-Perot observations of
589   comet Kohoutek, *Astrophys. J.*, *243*, 644-650
590 Tinsley, B. (1970), Temporal Variations in Geocoronal Balmer Alpha, *J. Geophys. Res. Space
591   Phys.*, *73*(13), 4139-4149
592 Woodward, R.C. (2013), personal communication.